SCIENCE CHINA
Information Sciences

• RESEARCH PAPER •

April 2025, Vol. 68, Iss. 4, 140408:1–140408:12
https://doi.org/10.1007/s11432-024-4323-6

Special Topic: Photonics Technology

Smart fiber-optic masks: real-time respiratory monitoring and health analysis

Qi YU[1], Ya-Nan ZHANG[1,2,3*], Jiaqi ZHANG[1], Shuang YANG[4], Lingxiao JIANG[1] & Xuegang LI[1,2,3]

[1]*College of Information Science and Engineering, Northeastern University, Shenyang 110819, China*
[2]*State Key Laboratory of Synthetical Automation for Process Industries, Northeastern University, Shenyang 110819 China*
[3]*Hebei Key Laboratory of Micro-Nano Precision Optical Sensing and Measurement Technology, Qinhuangdao 066004, China*
[4]*Affiliated Hospital of North Sichuan Medical College, Nanchong 637000, China*

Received 19 November 2024/Revised 3 January 2025/Accepted 21 February 2025/Published online 12 March 2025

Abstract In this study, we design a smart mask based on an ultrathin retractable flexible fiber optic sensor with high sensitivity (0.56 V/m^{-1}), ultra-light mass (0.24 g), and excellent tensile properties. The sensor was integrated with a medical mask to recognize multiple breathing patterns (standard, fast, slow, shallow, deep, breath-holding), coughing, and speaking, as well as to study gender characteristics and physiological differences in the respiratory system. By comparing the nasal-oral respiratory waveforms and frequencies, guidance for respiratory correction was provided. In addition, affixing flexible fiber optic sensors to the outside of the mask reduces the risk of cross-infection and significantly reduces temperature and humidity disturbances. Studies have shown that nine sensor locations placed on the outside of the mask responded significantly to respiratory waveforms. For personalized health management, the system is also equipped with a communication module, web and mobile apps to support data downloads, real-time monitoring, and exception alerts.

Keywords smart mask, respiratory monitoring, fiber optic sensor, health management, anti-interference

Citation Yu Q, Zhang Y-N, Zhang J Q, et al. Smart fiber-optic masks: real-time respiratory monitoring and health analysis. Sci China Inf Sci, 2025, 68(4): 140408, https://doi.org/10.1007/s11432-024-4323-6

1 Introduction

After the COVID-19 pandemic, respiratory infections pose a significant threat to human health. Patients who have been infected with the novel coronavirus sometimes experience long-term respiratory symptoms, such as chronic cough, dyspnea, and fatigue [1, 2], which may persist for months or even longer [3]. In severe cases, acute respiratory distress syndrome and pulmonary fibrosis are frequent complications that can result in prolonged lung function decline. Additionally, the rapid mutation of viral strains complicates prevention and control, though the primary symptom remains lung disease. Monitoring these symptoms over a long period of time helps to intervene and treat them in advance, thereby reducing the severity of the disease and the incidence of complications. Long-term, accurate, and portable respiratory measurements are critical in chronic disease management, telemedicine, and sports health. It can help to make timely adjustments to treatment regimens, remotely track health status, optimize exercise performance, and identify potential health problems in a timely manner. However, existing detection methods often suffer from difficulties in long-term monitoring, lack of accuracy, and poor portability [4]. Flexible wearable sensors break the limitations of traditional rigid devices and are more ergonomic, making users more willing to wear them for extended periods of time [5–10], but still face problems such as cross-infection and external interference [11]. Fiber optic sensors are commonly used in wearable devices because they are flexible and can transmit signals through light, making them resistant to external electromagnetic interference [12, 13]. It is capable of highly accurate measurements, sensitive to small physiological changes, and provides accurate data support. Fiber optic sensors provide continuous, non-invasive, and real-time monitoring of vital signs and health parameters [14]. Currently, fiber optic sensors have been employed to monitor various physiological parameters, including blood pressure [15], heart rate

* Corresponding author (email: zhangyanan@ise.neu.edu.cn)

[16,17], pulse [18,19], respiration [20,21], gesture recognition [22], and human motion recognition [23]. In addition, fiber optic sensors can measure multiple physiological signals simultaneously. For example, Yue et al. [24] employed microfiber Bragg gratings for real-time monitoring of wrist pulse, knuckle flexion, and body temperature. Mishra et al. [25] developed a U-type dual microfiber interferometer with a polydimethylsiloxane (PDMS) base for monitoring neck movement and body temperature in real-time. Shao et al. [26] integrated a fiber Bragg grating into a nylon bandage, creating a real-time system that monitors pulse and respiratory rate. The advancement of flexible fiber-optic wearable sensors offers a straightforward and efficient monitoring approach with uses in healthcare, motion detection, and human-machine interactions. In this study, we present a smart mask for real-time respiratory monitoring in everyday situations. The aim is to improve the accuracy and reliability of respiratory measurements while effectively preventing cross-infection and reducing external interference. The core sensing element of the smart mask is an ultrathin, flexible, and stretchable fiber optic curvature sensor. This sensor is low cost, small, flexible, cyclic, and lightweight. The sensor is very sensitive to bending caused by respiratory airflow. We fabricated smart masks that are resistant to interference from temperature, humidity, and sensor paste position. Wearing the smart mask monitors and analyzes a variety of breathing conditions, including standard, fast, slow, shallow, deep, breath-holding, coughing, and talking. Alarm alerts are also issued for abnormal conditions. This remote monitoring setup allows healthcare workers to limit close contact with patients and reduce the risk of infection. The significance of this study is to promote the advancement of respiratory health monitoring technology to provide more effective solutions for chronic disease management and personalized medicine.

2 Principles and methods

2.1 Sensor design

Figure 1(a) shows a smart mask's conceptual application, consisting of an ultra-thin, flexible, stretchable fiber-optic curvature sensor and a disposable medical mask. Smart masks can detect many types of breathing signals, alerting to abnormal signals such as choking. These signals can be received through portable devices such as smartphones. The ultra-thin, flexible, stretchable fiber-optic curvature sensor comprises a fiber-optic sensing structure and an encapsulation layer. The fiber optic sensing structure is created by bending the fiber into a parabolic form and securing it within a PDMS encapsulation layer, as shown in Figure 1(b). Thinner than a dollar coin (Figure 1(c)), this fiber optic curvature sensor is about 3 cm long, 1 cm wide (Figure 1(d)), weighs about 0.24 g (Figure 1(e)), and can be easily wrapped around the finger (Figure 1(f)), a design that not only ensures a comfortable fit, but also adapts to the face by fitting snugly around the face and adapting to facial movements while breathing, improving monitoring accuracy. A smart mask can be made by embedding this sensor into the outside or inside of a medical mask, as shown in Figure 1(g), respectively. The smart mask prototype is compact, simple to fabricate, and suitable for practical use scenarios.

2.2 Working principle

Since the airflow generated during breathing causes the sensor to bend, a bend-sensitive ultra-thin stretchable fiber-optic sensor has been developed to detect the changes caused by airflow during breathing. The schematic diagram in Figure 2(a) illustrates the fundamental operating mechanism of the ultra-thin, flexible, stretchable fiber curvature sensor. A single-mode fiber (SMF) will form a tapered transition region with a rapidly varying diameter and a tapered waist region with a uniform diameter after the tensile-taper treatment, as shown in the upper panel of Figure 2(a). In the non-adiabatic tapered transition region, the fundamental mode in the SMF will be partially coupled to the higher-order modes. Coupling occurs again when the fundamental mode and the higher-order mode are transmitted through the uniform-diameter waist region to another tapered transition region, where interference will occur under certain conditions due to the difference in the effective refractive indices of the fundamental mode and the higher-order mode. Since the interference of any complex mode can be broken down into the combination of interferences from two modes, only the interference between two modes is analyzed theoretically. The interference intensity is given by

$$I = I_1 + I_2 + 2\sqrt{I_1 I_2}\cos\frac{2\pi(\Delta n_{\text{eff}})}{\lambda}L, \tag{1}$$

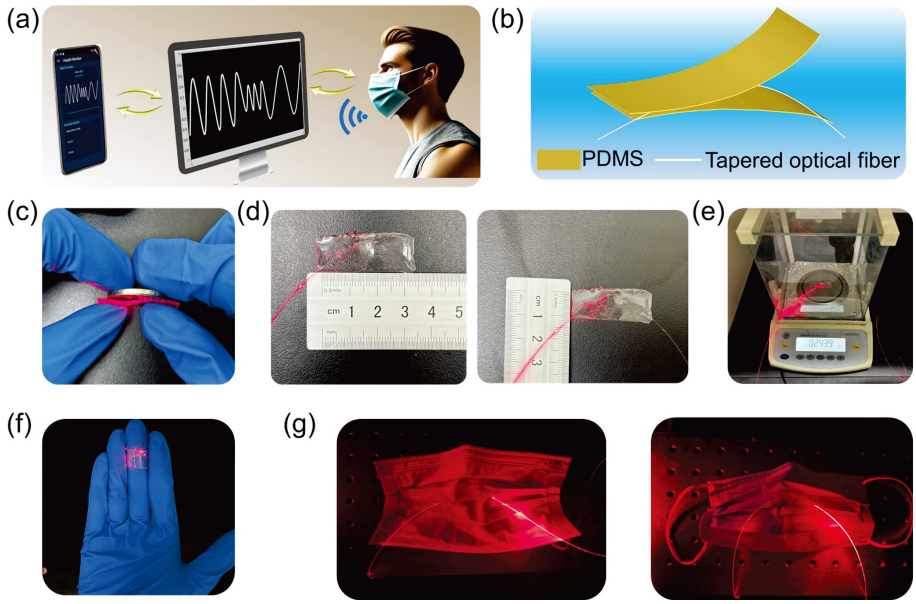

Figure 1 (Color online) (a) Wearable smart mask function: breathing data waveform can be displayed in real time on the mobile application; (b) fiber optic sensor structure; (c) fiber optic curvature sensor vs. the thickness of a sheet of a one-dollar coin; (d) length and width of the sensor; (e) weight of the sensor; (f) flexible stretchable sensor wrapped around a finger to demonstrate its softness; (g) sensing film placed on the inside and outside of the medical mask.

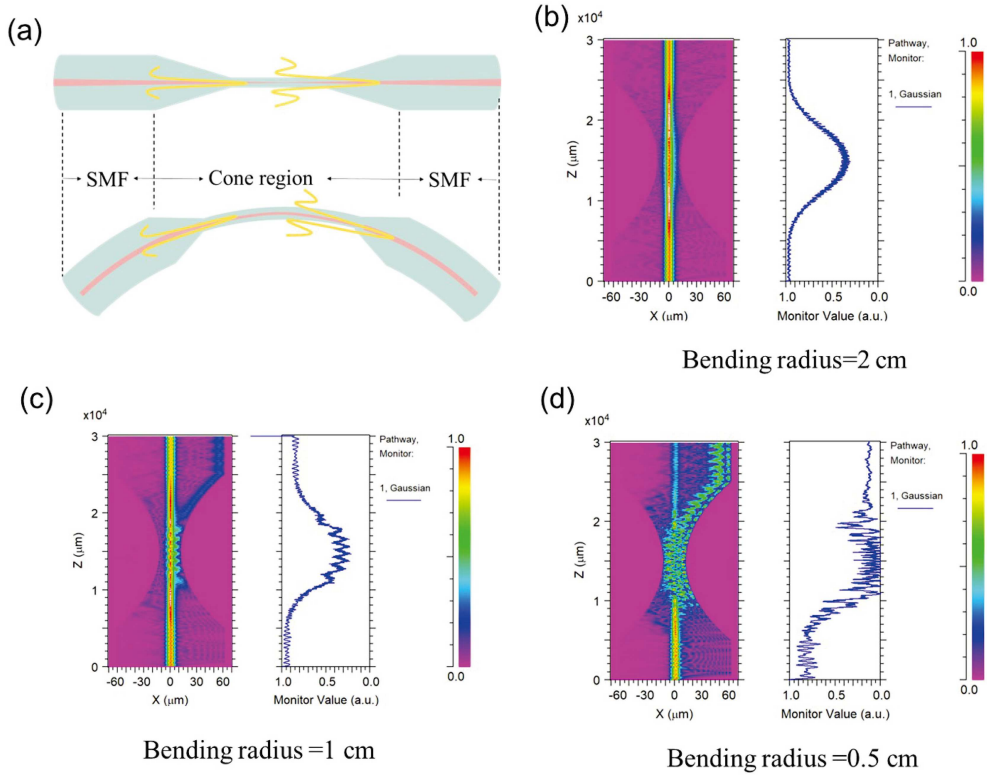

Figure 2 (Color online) (a) Sensing principle of tapered fiber curvature sensor; energy distribution of a tapered fiber core with a bending radius of (b) 2 cm (c) 1 cm (d) 0.5 cm.

where I_1 and I_2 denote the light intensity of two different order modes, respectively. L denotes the length of the sensing arm, i.e., the length of the tapered fiber. λ is the free space wavelength. Δn_{eff} denotes the difference in the effective refractive index between the two different order modes. When the airflow generated during breathing when bending occurs, Δn_{eff} will change, so the breathing waveform can be reflected in real-time by monitoring the intensity change. To prevent fiber breakage during stretching,

the tapered fiber is bent into a parabolic shape before encapsulation with PDMS, as shown in the lower panel of Figure 2(a). To study the effect of the diameter of the cone region on the light field distribution, the corresponding simulation model was built by RSoft in this experiment. It should be noted that in this study, we approximate the sensing region as part of a circular arc. We chose a bending radius of 2 cm, mainly because at this radius, the bending effect of the fiber is not yet too drastic. We analyzed the electric field distribution at different bending radii using the beam propagation method (BPM). Figure 2(b) shows the simulation results for a bending radius of 2 cm. The results show that when the energy of the optical signal gradually decreases from 1.0 to close to 0.3, the optical energy is mainly concentrated in the core region, indicating that at this bending radius, most of the optical energy remains within the core and the optical effect of the pulling cone begins to appear. As the optical signal is gradually coupled to the cladding region, the energy is further propagated outward. When the optical signal is re-coupled back to the core through the pull-cone region, a certain degree of loss occurs. Figures 2(c) and (d) show the simulations at bending radii of 1 and 0.5 cm, respectively. In both cases, the bending effect is more pronounced due to the smaller bending radius, and part of the optical energy leaks from the core to the cladding and couples with the optical energy in the core to form a resonant wave phenomenon. This phenomenon indicates that the smaller the bending radius, the more significant phase change occurs in the propagation of light waves within the fiber, leading to changes in the coupling between the light and thus affecting the transmission efficiency of the optical signal. By analyzing these simulation results, we find that a smaller bending radius (i.e., larger bending angle) significantly affects the propagation of light waves, especially the coupling process of optical signals between the core and cladding.

3 Experimental

3.1 Materials and experimental equipment

The standard single-mode optical fibers (size 9/125 μm) were manufactured by Changfei (Jinan, China) and exhibit low loss, bend insensitivity, excellent attenuation, and bending resistance. The PDMS polymer and curing agent (DC184) were purchased from Dow Corning, and the slides were purchased from Chiling (Jiangsu, China). The disposable medical masks were obtained from Shande Medical Devices (Hebei, China). The experimental setup includes the following equipment: a fiber optic fusion taper puller (Idealphotonics+IPCS5000), a thermostatic heating table (Hambone, HP-1515), a 1550 nm laser light source (CONQUER), a photodetector (PD) (Thorlabs, PDA30B2), a data acquisition card (DAQ) (NI, USB6009), and a personal computer (PC) with labview.

3.2 Tapered optical fiber production

First, the coating layer of the optical fiber was stripped using fiber optic pliers with a stripping length of 2 cm and then cleaned with anhydrous alcohol. Next, the optical fiber was placed on a fiber optic fusion taper puller (Idealphotonics+IPCS-5000), and the pre-stretched core and cladding material were heated to a high temperature using the flame generated by hydrogen combustion. Subsequently, two forces in opposite directions are applied to stretch the fiber so that the diameter of the fiber is gradually reduced. Tapered fibers with different diameters were fabricated by setting the length of the pulling cone for performance comparison.

3.3 Fabrication of a flexible stretchable optical fiber curvature sensor

Firstly, we mixed PDMS polymer and curing agent in the ratio of 10:1. Then, the mixture was placed for degassing at room temperature. Next, we uniformly applied the PDMS precursor to a custom-sized glass sheet. The glass sheet was placed on a heating table, and the temperature was set to 80°C. Then, the fabricated tapered optical fiber was placed on the glass sheet in a parabolic shape to be embedded in the PDMS. After heating for 40 min, the PDMS will be cured. Finally, the optical fiber is carefully removed from the mold, and we have an ultrathin flexible, stretchable optical fiber curvature sensor.

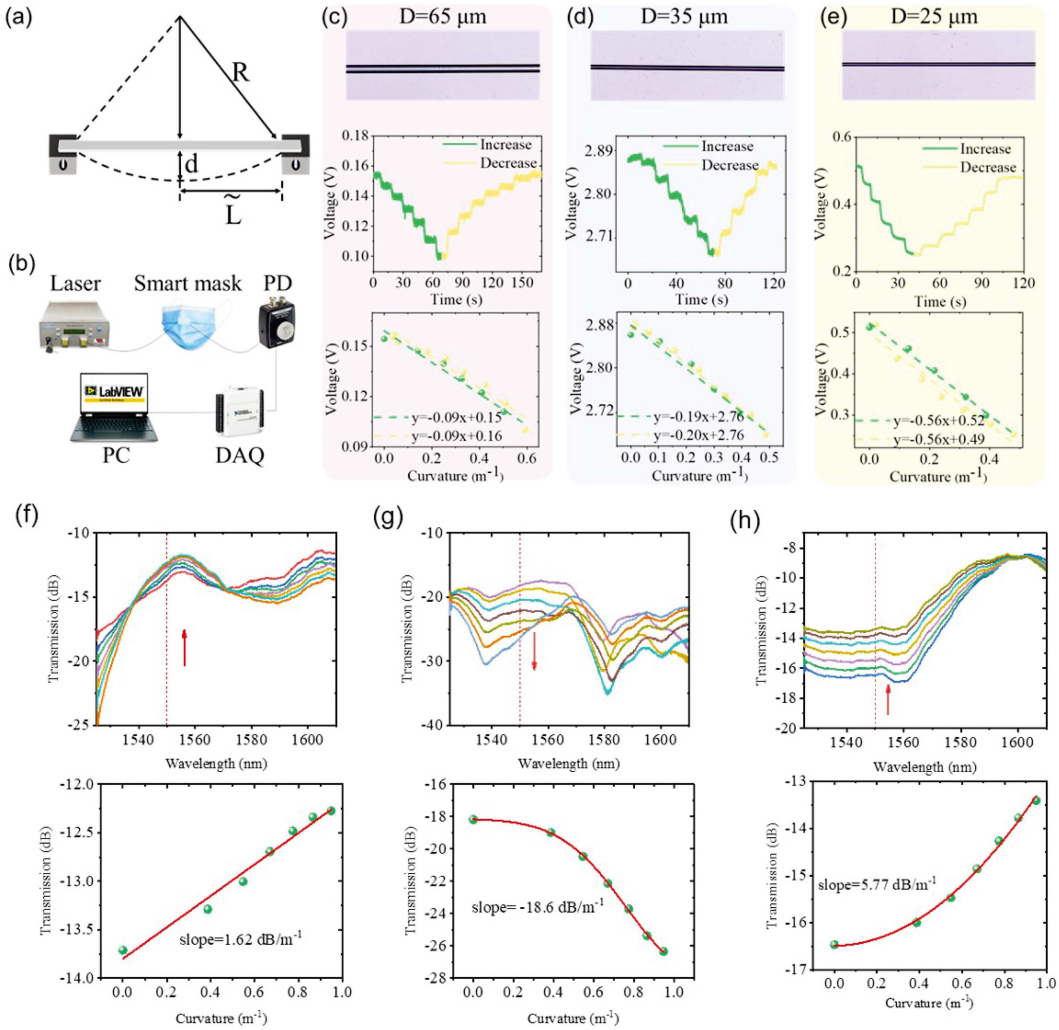

Figure 3 (Color online) (a) Curvature testing principle; (b) diagram of continuous monitoring system; (c)–(e) microscope diagrams, spectrograms, and sensitivities of taper diameters of 65, 35, and 25 μm, respectively; (f)–(h) spectral response for curvature radii of 1, 2, and 3 cm, respectively.

4 Results and discussion

4.1 Curvature test results

In the bending sensing experiment, the curvature measurement was performed using a spiral test stand, as shown in Figure 3(a). The sensing probe is placed on the surface of a steel ruler mounted on an adjustable platform. As the platform moves up and down, the probe bends into various curvatures, which are calculated based on the geometric relationship.

$$C = \frac{1}{R} = \frac{2d}{d^2 + \tilde{L}^2}, \tag{2}$$

where C is the curvature, R is the radius of curvature of the bend, $\tilde{L}$ is half of the distance between the adjustable platforms (here 15 cm), and d is the movement distance of the elevating platform. Therefore, the displacement of the elevating platform can be recorded to convert the curvature. The fiber curvature test system, shown in Figure 3(b), consists of a 1550 nm laser light source, an ultra-thin flexible and stretchable fiber curvature sensor, a PD, a DAQ, and a host computer running LabVIEW. The DAQ has 8 analog input channels, supports a maximum sampling rate of 48 kS/s with a 14-bit resolution to accurately acquire a variety of biological signals, and supports an input voltage range of ±10 V. The card has a USB interface with a high degree of compatibility for a variety of experimental needs. The card adopts a USB interface, which has high compatibility and is suitable for a variety of experimental needs.

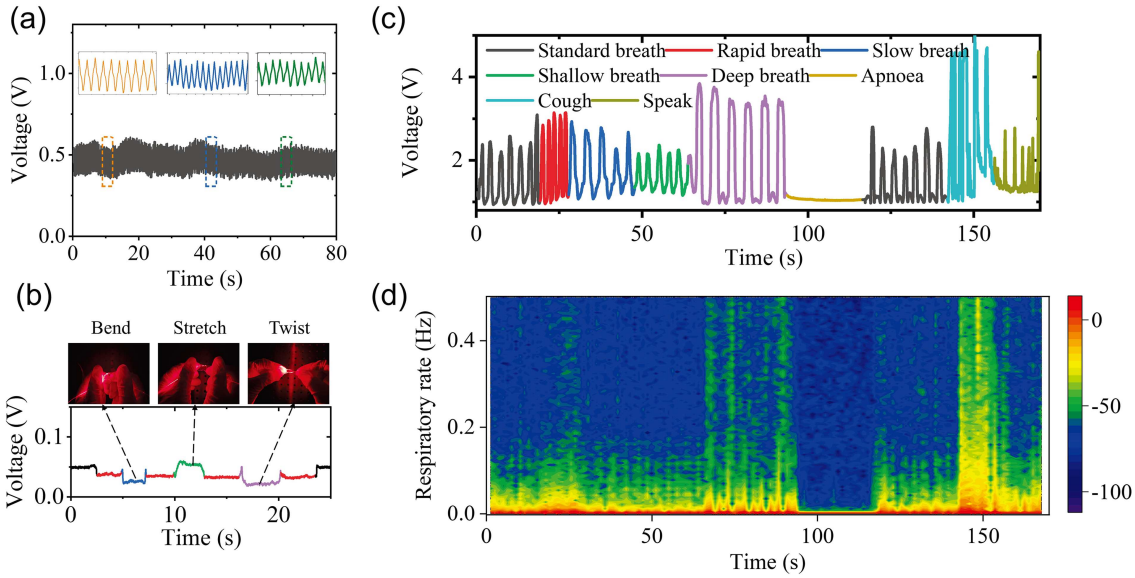

Figure 4 (Color online) (a) Repeat the stretching several times and randomly select three regions of spectral magnification maps to demonstrate its good cyclicity; (b) the sensing diaphragm can be restored to its original state after bending, stretching, and twisting; (c) continuously monitor waveforms of different respiratory modes; (d) instantaneous frequency maps of different respiratory modes.

The single-wavelength laser signal from the light source is converted into an electrical signal by the fiber optic sensor and transmitted to the host computer via the DAQ for further analysis and processing. The corresponding optical power will change when the fiber optic sensor is bent. In the curvature test, the optical fiber sensing probe is fixed to a steel ruler with good toughness, which is placed on top of the two magnetic holders. During the bending experiment, the spiral handle of the spiral test frame is rotated, which causes the spiral test frame to displace in the longitudinal direction and causes the steel ruler to bend, thus indirectly realizing the purpose of bending the optical fiber. To verify the effect of different diameters of fiber cones on the test results, we fabricated three diameters of fiber cones, 65, 35, and 25 μm, respectively. We carried out curvature tests on these three different diameters of fiber cones. After the bending-recovery process, we found an excellent linear relationship between the curvature change, the corresponding power change, and the recoverability, as shown in Figures 3(c)–(e). The curvature sensitivities of the three tapered fibers are 0.09, 0.20, and 0.56 V/m^{-1}, respectively, indicating that the smaller the fiber diameter, the higher the sensitivity. However, a minimal fiber diameter could result in a fragile structure in practical use. Therefore, selecting a 25 μm diameter is recommended as the optimal choice for the test structure. The bending radius of the parabola is also an important factor affecting the experimental results. We bent the 25 μm tapered optical fiber into different radii (1, 2, and 3 cm), and the spectral measurements are shown in Figures 3(f)–(h), respectively. The sensitivities in these cases are also compared. By analyzing the spectra when the bending radius was varied, we found that the highest sensitivity at 1550 nm was achieved when the radius of curvature was about 2 cm.

4.2 Breath test results

4.2.1 *Multi-functional breath test*

Since the fiber optic sensor undergoes a bending-recovery process during breathing, we performed rigorous bending tests on the flexible sensor diaphragm. After reaching thousands of bends, the recovery was observed, and the whole testing process is shown in Figure 4(a). We randomly selected three regions in the test and observed good repeatability of the waveforms, demonstrating the flexible sensor's stability after many bending cycles. Subsequently, we performed deformation experiments, including bending, stretching, and rotating, to simulate various scenarios that may occur while using the mask. We observed that the flexible sensors effectively returned to their initial state after these deformations, a result shown in Figure 4(b), which provides a reliable basis for their application in masks. An ultra-thin, flexible, and retractable fiber optic sensor is fixed on the medical mask (Hebei Shande Medical Equipment Co., Ltd.) with double-sided adhesive. In the breathing test experiment, the sampling frequency is 100 Hz.

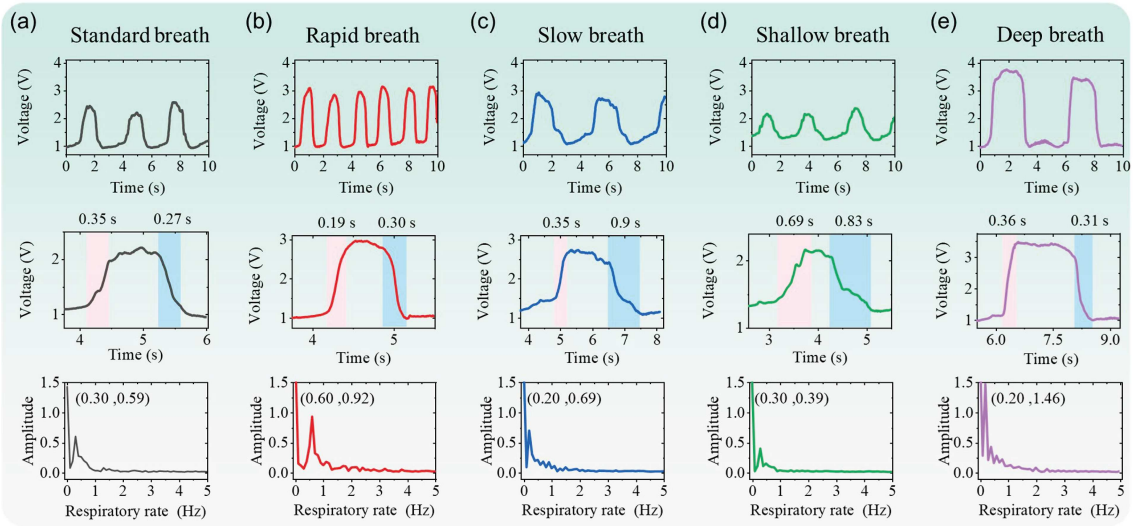

Figure 5 (Color online) Respiratory waveforms in 10 s for different modes, single cycle waveforms with rise time and recovery time, respiratory rate. (a) Standard breath; (b) rapid breath; (c) slow breath; (d) shallow breath; (e) deep breath.

The DAQ we chose fully meets this requirement, and its high sampling rate can ensure the accuracy and reliability of data collection. We chose healthy adult volunteers. After the volunteers were stabilized for 30 min, we put the smart mask on their faces for the test. In the process, we recorded waveform data when he performed different actions such as standard, fast, slow, shallow, deep, paused, coughing, and talking, as shown in Figure 4(c). Subsequently, we analyzed these waveform data in detail, especially for the change in respiratory transient frequency. Figure 4(d) illustrates a notable variation in the instantaneous frequency of respiration across different states. These findings provide strong data support for the further optimization of the respiratory monitoring system based on the built-in flexible sensors in the mask and also provide new possibilities for the clinical use of respiratory frequency changes to assist in the judgment of health conditions.

Waveforms of different respiratory states were analyzed individually over 10 s, including waveform plots of respiration, respiratory waveforms within a single cycle, and respiratory rate. Figure 5(a) represents normal respiration, with rise and recovery times of 0.35 and 0.27 s. Fast Fourier transform (FFT) was applied to the breathing waveform to convert the signal from the time domain to the frequency domain, allowing us to extract the dominant frequency component, which corresponds to the respiratory rate [27]. The respiratory rate measured using the FFT was 0.30 Hz. The normal respiratory rate of an adult is generally between 12 and 20 breaths per minute, which is consistent with the standard respiratory rate of an adult. Figure 5(b) represents rapid breathing; respiratory cycles increased significantly within 10 s, and the fastest rise time was 0.19 s. The respiratory rate was 0.60 Hz. Generally, shortness of breath is associated with strenuous exercise, cardiovascular disease, etc., so it should be taken seriously when the respiratory rate is greater than the standard respiratory rate. In such states, the respiratory rate is faster, and the rise time of the respiratory waveform becomes shorter, which may reflect a rapid increase in ventilation by the respiratory system to meet the body's oxygen demand in emergencies [28]. This phenomenon may also be associated with an increased burden on the heart, lungs, and other organs. Figure 5(c) represents slow breathing with a respiratory rate decreasing to 0.2 Hz. Slow breathing may be due to respiratory organ failure, craniocerebral injury, or pharmacologic factors. In addition to focusing on the underlying disease caused by the respiratory rate, respiration intensity is also necessary. Slow breathing is usually accompanied by long inhalation and exhalation times and may be accompanied by apnea, which needs to be diagnosed in conjunction with the patient's overall health [29]. Figures 5(d) and (e) show the results of shallow and deep breathing tests, respectively. The frequency of shallow breathing is 0.30 Hz, consistent with the frequency of normal breathing, but the amplitude is significantly lower. Shallow and slow respiration is when the respiration amplitude becomes shallow, and the respiratory rhythm slows down. It is a symptom of severe respiratory failure, usually due to the effects of the brain, lungs, thorax, and medication factors. Figure 5(e) shows the deep breathing process with rise time and recovery time of 0.36 and 0.31 s. The respiratory rate decreases during deep breathing because deep breathing implies an increase in the air volume in each breath, allowing more oxygen so that the body

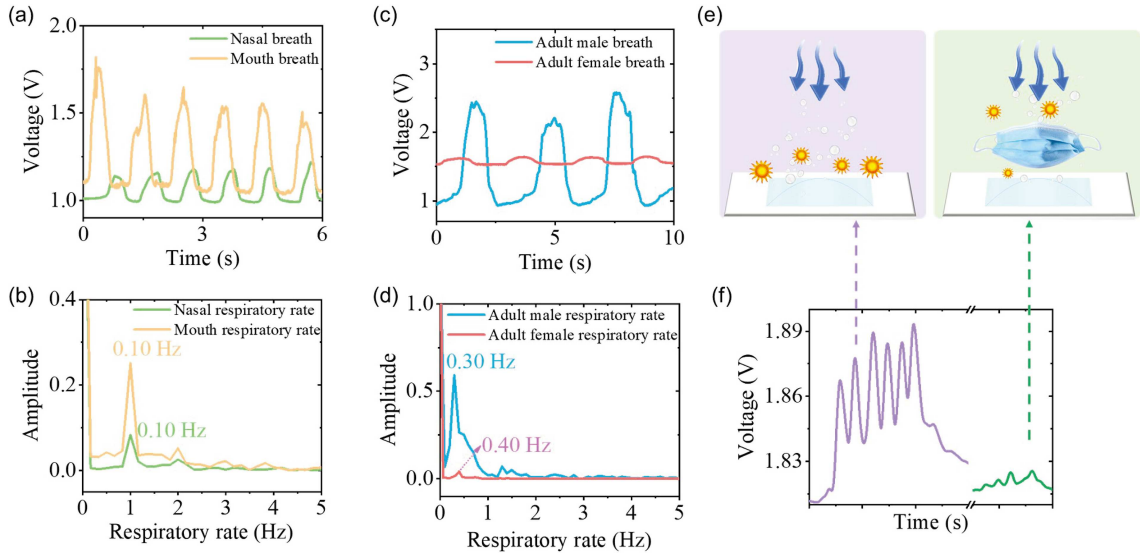

Figure 6 (Color online) (a) Comparison of nasal and oral respiration waveforms; (b) comparison of nasal and oral respiration frequencies; (c) comparison of respiration waveforms between adult males and females; (d) comparison of respiration frequencies between adult males and females; (e) schematic diagram of the effect of temperature and humidity of proximity respiration in the same position without and with a mask with the sensors fixed to the experimental platform; (f) comparison of waveforms without and with masks.

does not need to breathe as often to meet the oxygen demand.

Human breathing is categorized into nose breathing and mouth breathing. Usually, people breathe through the nose. When there is apparent nasal congestion or other lesions in the nasal cavity, people may breathe through the mouth, i.e., mouth breathing. Prolonged mouth breathing will result in air that is not effectively heated and moisturized, thus irritating the mucous membrane of the throat, causing symptoms such as dry mouth, sore throat, chronic cough, and even increasing the risk of respiratory tract infections in severe cases. Figure 6(a) shows a comparison of the waveforms of nasal and mouth breathing. When nasal and mouth breathing are performed at the same frequency, the amplitude of mouth breathing is more significant, as shown in Figure 6(b). This difference in amplitude can be attributed to the greater airflow in mouth breathing because it involves fewer channel restrictions compared to the nasal airway [30]. In addition, the absence of nasal resistance during mouth breathing may lead to faster and deeper inspiration, increasing the amplitude of the resulting respiratory waveform [31]. Gender differences may also affect the breathing results. Figure 6(c) shows that males can breathe deeper than females, which may be because males have a thicker and more muscular diaphragm, which creates a more significant pressure differential for deeper breathing. Figure 6(d) shows that females have a slightly faster respiratory rate, but the difference is insignificant. Although the difference was not statistically significant. This finding is consistent with previous research suggesting that, on average, women may breathe slightly faster than men due to metabolic differences and body size. Smaller body sizes and higher metabolic rates are typically associated with faster respiration rates, as the body requires more oxygen per unit of body weight [32]. However, as mentioned earlier, the observed differences in respiratory rate between the sexes are relatively small and may not be clinically significant.

4.2.2 *Anti-interference experiments*

During the experiment, we found that in addition to the curvature produced by respiration producing changes in the spectrum, the accumulation of temperature during respiration and the humidity of water vapor also affect the spectrum. In general, the temperature of human exhaled gas is about 36.5°C, and the humidity is about 95% relative humidity. In order to verify the effect of humidity and temperature produced by breathing on the spectra, we pasted the sensing diaphragm on a glass sheet and fixed it on the experimental platform. Then, we conducted two sets of experiments: breathing on the sensor at a close distance vertically without and with a mask, respectively, as shown in Figure 6(e). Spectra were obtained as shown in Figure 6(f). We found that the spectral amplitude of the latter was significantly lower than that of the former. Considering that the sensor is fixed on a glass sheet, there is no curvature effect, and this difference is mainly caused by the temperature and humidity generated by breathing. It can thus be

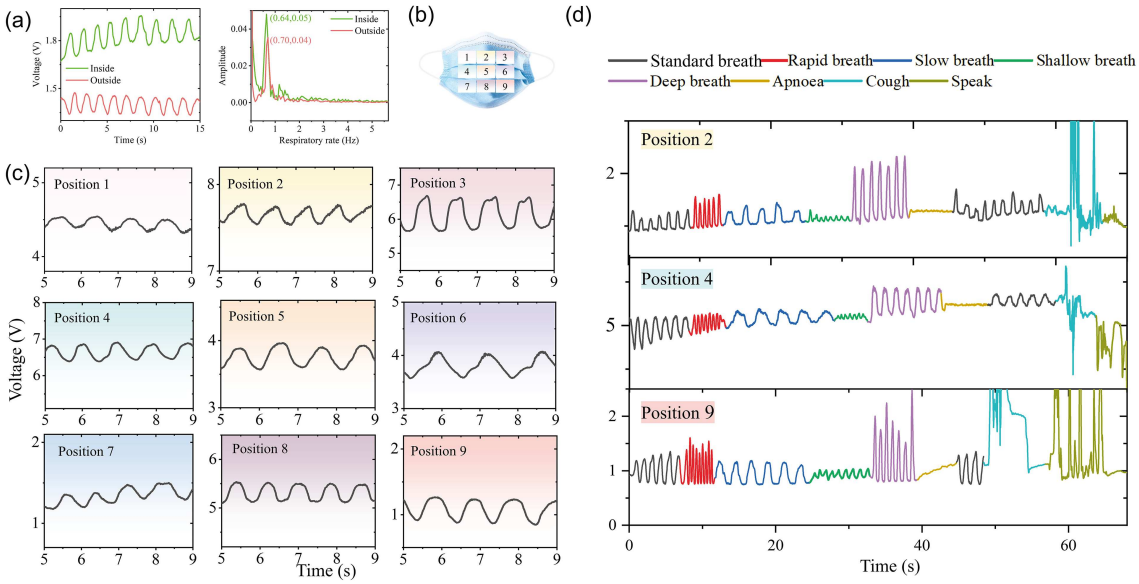

Figure 7 (Color online) (a) Comparison of waveforms at the same position when the sensor is pasted on the inside and outside of the mask; (b) division of 3×3 grid area on the outside of the medical mask; (c) respiratory waveform variations can be sensed well when the sensors are placed in 9 positions, respectively, which proves that the sensors are insensitive to the position of the pasting; (d) multifunctional breath test results at different locations.

shown that disposable medical masks can insulate part of the humidity and temperature. Therefore, we chose to paste the sensing patch outside the medical mask. Doing so reduces both interference and the risk of cross-infection.

To verify the effect of pasting flexible fiber optic sensors on the inside and outside of medical masks on the test results, we conducted comparative experiments. As shown in Figure 7(a), it is found that the baseline drift of the waveform amplitude when pasted on the inner side of the mask is caused by the influence of temperature and humidity. Moreover, the absolute value of the waveform amplitude generated when pasted on the inside of the mask is higher than that on the outside. However, this discrepancy can be resolved by normalizing the data since we are concerned with the contrast of the waveforms rather than the amplitude. Further analyzing the frequencies of the two pasting positions, we obtained a relationship between respiratory frequency and amplitude. The coordinates of the medial and lateral pastes were (0.64, 0.05) and (0.70, 0.04), respectively. This slight difference may be due to the inability of the tester to control the frequency of each breath to remain consistent precisely. In conclusion, pasting on the outside and inside of the mask did not affect the results of the breath test. Therefore, we chose to affix the sensor to the outside of the mask, which ensured the sensor's performance and made it resistant to humidity and temperature disturbances during breathing. This also reduces the risk of cross-infection and can be reused.

To determine whether it is necessary to stick the flexible sensor close to the nose to obtain suitable respiratory waveforms, we divided the outer side of the mask into nine rectangular areas of 2 cm×3 cm in size, as shown in Figure 7(b). Then, we pasted the sensors into these nine areas of the mask for respiration testing and obtained the nine waveforms shown in Figure 7(c). It should be emphasized that the waveforms in Figure 7(c) are raw data without any processing. Then, we randomly selected three different positions above the middle position, on the left side, and on the lower right side for testing. From the results in Figure 7(d), we found that the sensor placed in any area can respond well to the respiratory waveform.

4.3 Portable personality health monitoring

As shown in Figure 8, to realize portable monitoring, we integrated the hardware in an arms package. We realized data download, real-time monitoring, and abnormal alerts through the communication module with the accompanying webpage and cell phone application. The cell phone app designed based on this framework can monitor the data in real time, and users can view the waveform, respiratory rate, and other essential parameters. In addition, when the wearer's breathing pattern is detected to be abnormal, the

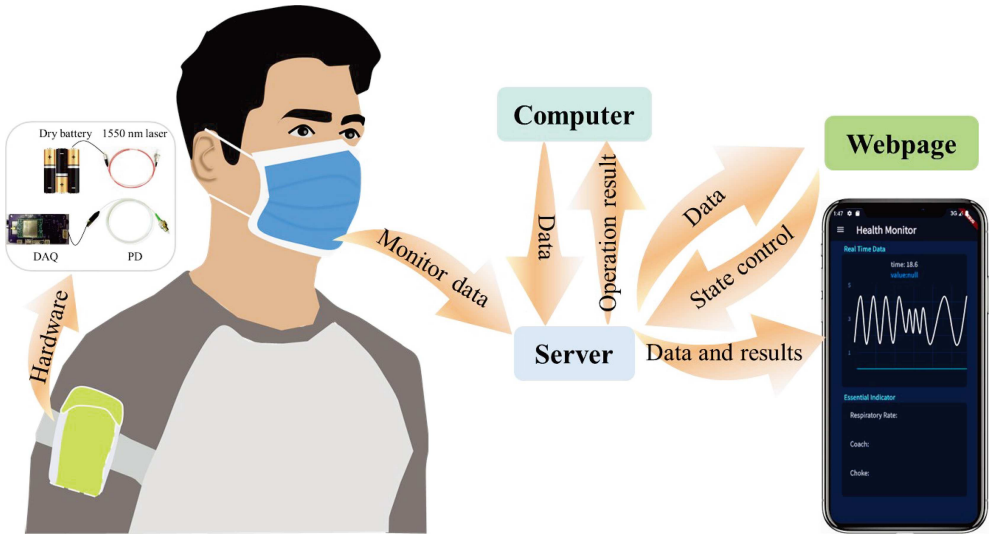

Figure 8 (Color online) Integrated portable smart mask application.

Table 1 Fiber optic breathing sensor performance comparison.

Sensor structure	Detection parameter	Integrated platform	Rise time (s)	Recovery time (s)	Anti-interference test	Ref.
Surface plasmon resonance	Humidity	–	0.44	0.86	Temperature	[33]
Fiber Bragg gratting	Humidity	Subnasal devices	44.4	111.7	–	[34]
Asymmetric fiber	Humidity	–	0.56	0.31	Temperature	[35]
Tilted fiber grating	Humidity	–	0.042	0.115	–	[36]
SMF-multimode fiber-SMF	Curvature	Oxygen mask	–	–	–	[37]
SMF-multimode fiber-SMF	Curvature	Textile tape	–	–	Temperature	[38]
Microspheres coupling	Curvature	–	0.028	0.027	Temperature	[39]
Parabolic Tapered Fiber	Curvature	–	0.35	0.27	Temperature, humidity, paste position	This work

application will issue an alarm in time to realize personalized monitoring. This way, users can easily use the system and get help quickly, whether monitoring their health or dealing with unexpected situations. Please refer to the supporting materials for the portable smart mask's real-time display function.

5 Conclusion

This study proposes a smart mask that uses a fiber optic sensor as a sensing element to enable monitoring of the breathing process. The sensor utilizes the curvature change caused by exhalation to sense the respiratory state. It is characterized by ultra-thin, flexible, high sensitivity, and fast rise time (0.19 s). After comparing the sensing performance of tapered optical fibers with different diameters, we chose a tapered optical fiber with a diameter of 25 μm as the test sensor. The sensor could recognize the waveforms of various states such as standard, fast, slow, shallow, deep, breath-holding, coughing, and speaking. We also compared the waveforms of nasal and mouth breathing and breathing of different genders. The experiments demonstrated that the sensor affixed to the outside of the mask could mitigate the effects of humidity and temperature on the spectra and accurately respond to the respiratory waveforms. At the same time, we verified the waveform recognition performance of the sensor affixed to the outside of the mask at different positions, and the results showed that the different positions had little effect on the experimental results. To realize real-time respiratory monitoring, we implemented portable monitoring by integrating the hardware and using the communication module and the accompanying web page and mobile application to realize data download, real-time monitoring, and abnormal situation alerts. This

operation facilitates the back-end processing of the smart mask. In Table 1 [33–39], we compare fiber-optic respiratory sensors with different sensing principles, and the results show that our study integrates a number of factors, including rise time, recovery time, integration with wearable platforms, and immunity to interference. This research provides technical support for the development and wide application of smart masks and promotes the development of smart wearable devices in the fields of health monitoring, exercise surveillance, and disease prevention.

Acknowledgements This work was supported in part by National Natural Science Foundation of China (Grant Nos. 62222504, 62475040, 62375045), Liaoning Revitalization Talents Program (Grant No. XLYC2203125), and Natural Science Foundation of Liaoning Province (Grant No. 2023021199-JH26/103).

Supporting information The supporting information is available online at info.scichina.com and link.springer.com. The supporting materials are published as submitted, without typesetting or editing. The responsibility for scientific accuracy and content remains entirely with the authors.

References

1 Alberici F, Delbarba E, Manenti C, et al. A report from the Brescia Renal COVID task force on the clinical characteristics and short-term outcome of hemodialysis patients with SARS-CoV-2 infection. Kidney Int, 2020, 98: 20–26
2 Hennigs J K, Huwe M, Hennigs A, et al. Respiratory muscle dysfunction in long-COVID patients. Infection, 2022, 50: 1391–1397
3 Hall S. Vaccines reduce the risk of long COVID in children. Nature, 2024, 625: 227
4 Zhen Z, Li Z, Zhao X, et al. Formation of uniform water microdroplets on wrinkled graphene for ultrafast humidity sensing. Small, 2018, 14: 1703848
5 Iqbal M H, Aydin A, Brunckhorst O, et al. A review of wearable technology in medicine. J R Soc Med, 2016, 109: 372–380
6 Jayathilaka W A D M, Qi K, Qin Y, et al. Significance of nanomaterials in wearables: a review on wearable actuators and sensors. Adv Mater, 2019, 31: 1805921
7 Lu W, Zhang Q, Liu N, et al. Nylon fabric/GO based self-powered humidity sensor based on the galvanic cell principle with high air permeability and rapid-response. Small, 2024, 20: 2306463
8 Lai Q T, Zhao X H, Sun Q J, et al. Emerging MXene-based flexible tactile sensors for health monitoring and haptic perception. Small, 2023, 19: 2300283
9 Wang T, Guo Y, Wan P, et al. Flexible transparent electronic gas sensors. Small, 2016, 12: 3748–3756
10 He J, Li S, Hou X J, et al. A non-contact flexible pyroelectric sensor for wireless physiological monitoring system. Sci China Inf Sci, 2022, 65: 122402
11 Lu C F, Wu S, Zhang Y Y, et al. Electromechanical modeling of eye fatigue detecting using flexible piezoelectric sensors. Sci China Inf Sci, 2018, 61: 060417
12 Peng X L, Yang Z Y, Peng B, et al. In situ plasmonic & electrochemical fiber-optic sensor for multi-metal-ions detection. Sci China Inf Sci, 2024, 67: 112406
13 Li Z, Yuan J, Rao L, et al. Ultrasensitive refractive index and temperature sensor based on D-shaped photonic crystal fiber by group birefringence response in a Sagnac interferometer. Photonics Nanostruct-Fund Appl, 2024, 61: 101291
14 Jha R, Mishra P, Kumar S. Advancements in optical fiber-based wearable sensors for smart health monitoring. Biosens Bioelectron, 2024, 254: 116232
15 Li L, Sheng S, Liu Y, et al. Automatic and continuous blood pressure monitoring via an optical-fiber-sensor-assisted smartwatch. PhotoniX, 2023, 4: 21
16 Li L, Yang C, Wang Z, et al. Stretchable polymer optical fiber embedded in the mattress for respiratory and heart rate monitoring. Optics Laser Tech, 2024, 171: 110356
17 Zhao T, Fu X, Zhou Y, et al. Noncontact monitoring of heart rate variability using a fiber optic sensor. IEEE Internet Things J, 2023, 10: 14988–14994
18 Wang X, Zhou H Y, Chen M H, et al. Wearable ultrasensitive and rapid human physiological monitoring based on microfiber Sagnac interferometer. Sci China Inf Sci, 2024, 67: 132403
19 Guo Y, Wang W, Shi G, et al. Optical smart wearable sensor: pulse waveform and pulse rate monitoring with a flexible loop optic-microfiber. J Lightwave Technol, 2025, 43: 1462–1468
20 Liu S, Yan W, Zhong J, et al. Compact breath monitoring based on helical intermediate-period fiber grating. Sens Actuat B-Chem, 2022, 369: 132372
21 Nedoma J, Kostelansky M, Vilimek D, et al. Fiber-optic breathing mask: an alternative solution for MRI respiratory triggering. IEEE Trans Instrum Meas, 2022, 71: 1–13
22 Li J, Liu B, Hu Y, et al. Plastic-optical-fiber-enabled smart glove for machine-learning-based gesture recognition. IEEE Trans Ind Electron, 2023, 71: 4252–4261
23 Wang S, Liu B, Wang Y L, et al. Machine-learning-based human motion recognition via wearable plastic-fiber sensing system. IEEE Internet Things J, 2023, 10: 17893–17904

24 Yue X, Lu R, Yang Q, et al. Flexible wearable optical sensor based on optical microfiber Bragg grating. J Lightwave Technol, 2022, 41: 1858–1864

25 Mishra P, Kumar H, Sahu S, et al. Flexible and wearable optical system based on u-shaped cascaded microfiber interferometer. Adv Mater Technol, 2023, 8: 2200661

26 Shao T P, Liu Z C. Design of pulse and respiration monitoring system based on fiber optic sensing and VMD-FPR processing algorithm. Optical Fiber Tech, 2022, 73: 103033

27 Feng D, Zheng H, Sun H, et al. SnO_2/polyvinyl alcohol nanofibers wrapped tilted fiber grating for high-sensitive humidity sensing and fast human breath monitoring. Sens Actuat B-Chem, 2023, 388: 133807

28 van Vliet T, Casciaro F, Demaria M. To breathe or not to breathe: understanding how oxygen sensing contributes to age-related phenotypes. Ageing Res Rev, 2021, 67: 101267

29 Losurdo A, Vollono C, Mazza S, et al. Asymptomatic bradyarrhythmia and obstructive sleep apnea. Sleep Biol Rhythms, 2014, 12: 305–307

30 Araújo B C L, de Magalhães Simões S, de Gois-Santos V T, et al. Association between mouth breathing and asthma: a systematic review and meta-analysis. Curr Allergy Asthma Rep, 2020, 20: 24

31 Izuhara Y, Matsumoto H, Nagasaki T, et al. Mouth breathing, another risk factor for asthma: the Nagahama study. Allergy, 2016, 71: 1031–1036

32 Gargaglioni L H, Marques D A, Patrone L G A. Sex differences in breathing. Comp Biochem Physiol Part A-Mol Integr Physiol, 2019, 238: 110543

33 Wang Y, Wang J, Shao Y, et al. Highly sensitive surface plasmon resonance humidity sensor based on a polyvinyl-alcohol-coated polymer optical fiber. Biosensors, 2021, 11: 461

34 Presti D L, Massaroni C, Zaltieri M, et al. A magnetic resonance-compatible wearable device based on functionalized fiber optic sensor for respiratory monitoring. IEEE Sens J, 2021, 21: 14418–14425

35 Shao M, Zhang R, Zhao X, et al. Dual-core fiber based in-line Michelson interferometer for humidity sensing. Optical Fiber Tech, 2021, 64: 102570

36 Jiang B, Bi Z, Hao Z, et al. Graphene oxide-deposited tilted fiber grating for ultrafast humidity sensing and human breath monitoring. Sens Actuat B-Chem, 2019, 293: 336–341

37 Li X, Liu D, Kumar R, et al. A simple optical fiber interferometer based breathing sensor. Meas Sci Technol, 2017, 28: 035105

38 Cao Z, Shao M, Yuan Y, et al. In-fiber Mach-Zehnder interferometer for wearable respiration measurement. Sens Actuat A-Phys, 2023, 364: 114806

39 Jiang C, Dai P, Li X, et al. Flexible wearable microfiber respiratory sensor based on microspheres coupling. IEEE Sens J, 2023, 23: 27324–27330